Chemical Geology 648 (2024) 121939

Contents lists available at ScienceDirect

Chemical Geology

journal homepage: www.elsevier.com/locate/chemgeo

A new experimental monazite-xenotime thermometer: Application to metamorphic environments

Wriju Chowdhury [a,b,*], Dustin Trail [a]

[a] Department of Earth and Environmental Sciences, University of Rochester, Rochester, NY 14627, USA
[b] Department of Mineral Sciences, National Museum of Natural History, Smithsonian Institution, Washington, DC, United States of America

ARTICLE INFO

Editor: Claudia Romano

Keywords:
Rare-earth phosphates
Monazite
Xenotime
Thermometry
Metamorphism

ABSTRACT

Monazite and xenotime are common metamorphic phases that may be reliably U/Th-Pb dated to obtain absolute ages. The utility of these minerals is significantly enhanced if a crystallization thermometer can be developed and applied to better establish the temperature-time (T-t) paths of crustal terranes. Here we report experiments in which we have modeled the T-dependent Rare Earth element (REE) cationic exchange between coexisting monazite and xenotime to derive a new thermometer. We present a thermometer in which phosphates were co-crystallized from 1150 °C to 850 °C at 1 GPa in a Y-REE-P_2O_5-NaCl-H_2O system, with oxygen fugacity buffered at the Ni-NiO equilibrium. The composition of the phosphates was quantified using a laser ablation inductively coupled plasma mass spectrometer (LA-ICP-MS). Results reveal strong correlations between $log_{10}\left(\frac{\prod X_{Xnt}^{LREE} \times X_{Mzt}^{Y}}{\prod X_{Mzt}^{LREE} \times X_{Mzt}^{Y}}\right)$ (at. %) and 10^4/T(K) and our preferred calibration is:

$$log\left(\frac{\prod X_{Xnt}^{LREE} \times X_{Mzt}^{Y}}{\prod X_{Mzt}^{LREE} \times X_{Mzt}^{Y}}\right) = \frac{(-6714 \pm 2264)}{T\ (K)} - (0.79 \pm 1.76)$$

where LREE = La, Ce and Pr, α = activity of a cation in a phase, and $\prod \alpha_{Mzt/Xnt}^{Y/REE}$ refers to the product of activities of Y and/or REEs in a phosphate phase. The errors are 2 s.e. The greatest strength of this thermometer is its versatility. One can obtain derivative thermometers based on select elements rather than the entire suite of REEs. We showcase our thermometer's adaptability by applying it to two studies that have published REE data on monazite and xenotime from some quartzo-feldspathic psammites and garnet-bearing pelites that experienced amphibolite facies metamorphism from the Naver nappe in the Northern Highlands Terrane, Scotland. The main calibration shown above, as well as four derivative single-element thermometers (Y, La, Ce and Pr) were applied to the first study. Upon applying these thermometers, we find that the calculated metamorphic Ts agree well with the regional metamorphic facies. Thus, this versatile thermometer can be used in geologic environments where monazite and xenotime co-crystallized.

1. Introduction

To unravel the geologic history of terranes, quantifying the thermodynamic conditions (T, P, fO_2, etc.) of the rocks during their formation and modification is crucial. Toward this end, petrologists and geochemists have developed multiple thermometers that use spatial petrographic relationships as well as experimentally derived phase-equilibria relationships (Ferry and Spear, 1978; Graham and Powell, 1984; Elkins and Grove, 1990; Ghiorso and Sack, 1991; Ferry and Watson, 2007; Thomas et al., 2010). However, there are very few phases that record metamorphic conditions and can be reliably dated to create a T-t path (e.g., zircon, garnet, phosphates, etc. are often used as datable thermobarometers (Pyle et al., 2001; Seydoux-Guillaume et al., 2002; Stowell et al., 2001; Tomkins and Pattison, 2007; Taghipour et al., 2015;

* Corresponding author at: Department of Mineral Sciences, National Museum of Natural History, Smithsonian Institution, Washington, DC, United States of America.
E-mail address: chowdhuryw@si.edu (W. Chowdhury).

https://doi.org/10.1016/j.chemgeo.2024.121939
Received 5 March 2023; Received in revised form 3 January 2024; Accepted 14 January 2024
Available online 24 January 2024
0009-2541/Published by Elsevier B.V.

Laurent et al., 2018; Mako et al., 2019 and Mako et al., 2024, and Shrestha et al., 2019, Kohn et al., 2017).

Here we present a calibration of log [REE] (Rare-Earth Element) partitioning between monazite and xenotime as a function of 10^4/T. This calibration may be used as a thermometer and applied to rocks in which monazite and xenotime co-crystallized. We investigate REE partitioning by experimentally synthesizing monazite and xenotime and quantifying the cationic exchange between these phases. These phases are common metamorphic minerals that host measurable quantities of U/Th and radiogenic Pb and thus can be robustly dated (Spear and Pyle, 2002; Harrison et al., 2002; Fletcher et al., 2004; Kohn and Vervoort, 2008). Monazite-xenotime thermometry has been explored previously (Heinrich et al., 1997; Gratz and Heinrich, 1997, 1998; Andrehs and Heinrich, 1998; Pyle et al., 2001; Seydoux-Guillaume et al., 2002; Mogilevsky, 2007) and thermometers developed by Heinrich et al., 1997, Gratz and Heinrich, 1997 and Andrehs and Heinrich, 1998 have been applied to natural phosphates (Viskupic and Hodges, 2001; Janots et al., 2008; Rasmussen et al., 2011a, 2011b; Laurent et al., 2018; Mako et al., 2019). Heinrich et al., 1997 developed their thermometer using natural, co-existing monazite and xenotime from pelites. Gratz and Heinrich, 1997 designed a thermometer by synthesizing phosphates in a Ce-Y-P-O system, while Andrehs and Heinrich, 1998 did the same in a system closer to natural REE concentrations.

The experimental studies (Heinrich et al., 1997; Gratz and Heinrich, 1997; Andrehs and Heinrich, 1998) were important since they were initial explorations into a system with such great potential, but there are also some major inconsistencies across the two experimental studies. In one study, the authors propose the pressure dependence of cationic exchange (Gratz and Heinrich, 1997) while in the other, there does not seem to be any pressure dependence (Andrehs and Heinrich, 1998). Secondly, neither study shows a strong T dependence for Ce(+LREE) partitioning into xenotime.

We have experimentally derived our thermometer at 1 GPa, by co-synthesizing the two phases in a water-saturated Y + La-Ce-Pr-Sm-Eu-Gd-Dy-Lu-U-Th-NaCl-P-O system using an end-loaded piston cylinder (PC) device at various Ts (850 to 1150 °C). We buffered the oxygen fugacity (fO_2) of the experiments using a Ni-NiO (NNO) mineral redox buffer (O'Neill and Pownceby, 1993). This redox buffer is about 0.8 log units more oxidizing than the Fayalite-Magnetite-Quartz (FMQ) buffer. We then calibrated the cationic exchange against 10^4/T, between these two phases by making LA-ICP-MS measurements of LREE (light REE viz., La + Ce + Pr + Sm + Eu) and Y + HREE (Heavy REE viz. Gd + Dy + Lu) in monazite and xenotime. Our main calibration was designed using the concentrations of Y, La, Ce, Pr and Gd. These elements showed the greatest sensitivity to T as well as the greatest R^2 values out of the entire REE suite and thus we selected them.

Subsequently, we tested our thermometer by applying it to published REE contents of monazite and xenotime from quartzo-feldspathic psammites and garnet-bearing pelites from the Northern Highland terrane in Scotland (Ashley et al., 2015; Mako et al., 2019). The phosphates analyzed in this study are coeval and we have done a further check for chemical equilibrium in a later section.

For this case study, we find a deviation of around 100 °C between our T (471–540 °C) estimates and those reported by Mako et al., 2019 (595–666 °C) who used the empirical thermometer published by Heinrich et al., 1997. We also derived the metamorphic T separately using four single element thermometers; $logD_{Y}^{Mzt/Xnt}$ (426–576 °C), $logD_{La}^{Mzt/Xnt}$ (480–540 °C), $logD_{Ce}^{Mzt/Xnt}$ (420–497 °C) and $logD_{Pr}^{Mzt/Xnt}$ (492–568 °C); all vs. 10^4/T (K), where $D_{REE}^{Mzt/Xnt} = \frac{[REE]^{Mzt}\ (at.\%)}{[REE]^{Xnt}\ (at.\%)}$. All the thermometers here present broadly similar results.

2. Material and methods

2.1. Theoretical background

The exchange reaction for the system can be represented by:

$$(LREE)PO_4^{Mzt} + (Y+HREE)PO_4^{Xnt} \leftrightarrow (LREE)PO_4^{Xnt} + (Y+HREE)PO_4^{Mzt} \quad (1)$$

Where LREE = La, Ce and Pr and HREE = Gd, Dy and Lu.

For (Eq. (1)), the reaction constant (K) is:

$$K = \frac{\prod\alpha_{Xnt}^{LREE} \times \prod\alpha_{Mzt}^{Y,HREE}}{\prod\alpha_{Mzt}^{LREE} \times \prod\alpha_{Xnt}^{Y,HREE}} \quad (2)$$

Where, α = activity of a cation in a phosphate phase, LREE = La, Ce and Pr and $\prod\alpha_{Phosphate}^{Y/REE}$ refers to the product of activities of Y and/or REEs in a phosphate phase.

This can be written as:

$$e^{\left[\sum -\Delta G^0_{REE}/RT\right]} = \frac{\prod\alpha_{Xnt}^{LREE} \times \prod\alpha_{Mzt}^{Y,HREE}}{\prod\alpha_{Mzt}^{LREE} \times \prod\alpha_{Xnt}^{Y,HREE}} \quad (3)$$

where R = gas constant, T = temperature (K), and ΔG^0 is the Gibbs free energy change for Eq. (1) when the two phases are in their standard states.

If Henrian behavior can be assumed:

$$\prod\alpha_{Xnt}^{LREE} = \left(\prod\gamma_{Xnt}^{LREE} \times \prod X_{Xnt}^{LREE}\right) \quad (4a)$$

$$\prod\alpha_{Xnt}^{Y,HREE} = \left(\prod\gamma_{Xnt}^{Y,HREE} \times \prod X_{Xnt}^{Y,HREE}\right) \quad (4b)$$

$$\prod\alpha_{Mzt}^{LREE} = \left(\prod\gamma_{Mzt}^{LREE} \times \prod X_{Mzt}^{LREE}\right) \quad (4c)$$

$$\prod\alpha_{Mzt}^{Y,HREE} = \left(\prod\gamma_{Mzt}^{Y,HREE} \times \prod X_{Mzt}^{Y,HREE}\right) \quad (4d)$$

where γ = activity coefficient of cationic exchange between monazite and xenotime and X_{Xnt}^{LREE} and $X_{Mzt}^{Y,HREE}$is the concentration (at. %) of LREE in xenotime and Y, HREE in monazite respectively.

Combining (Eqs. (3)) and (4) for all REE we obtain the relationship:

$$log\left(\frac{\prod X_{Xnt}^{LREE} \times \prod X_{Mzt}^{Y,HREE}}{\prod X_{Mzt}^{LREE} \times \prod X_{Xnt}^{Y,HREE}}\right) = \sum -\Delta G^0_{REE}\Big/_{2.303RT} - log\left(\prod\gamma_{REE}\right) \quad (5)$$

Thus, the left side of Eq. (5) should be linearly and negatively correlated with 1/T(K) assuming the ratio of $\prod\gamma_{REE}$ terms remain constant.

2.2. Piston cylinder experiments

We synthesized the experimental phosphates in a NaCl-bearing, water-saturated system: La-Ce-Pr-Sm-Eu-Gd-Dy-Lu-Y-P-U-Th-O which broadly and qualitatively bears chemical similarity to natural systems. To emulate natural metamorphic fluids, we added NaCl (Rauchenstein-Martinek et al., 2016; Yardley, 2013). To make the experimental charge, we mixed reagent-grade Y, REE and actinide salts (Table 1) in an agate mortar. We then loaded a portion of this mix along with crystalline H_3PO_4, NaCl, and 18.2 MΩ·cm H_2O (Table 2) into a 5 mm Pt capsule.

The Pt capsule was inserted into an oxidized Ni bucket with NiO powder + H_2O. Afterward, a 0.1 mm thick Pt sheet was cut to cover the capsule, and a 2 mm thick oxidized Ni lid was placed on top of the sheet. This entire assembly was put into a fired pyrophyllite bucket and placed into a graphite furnace, inside a borosilicate sleeve, girdled at the top and bottom by MgO filler pieces. This whole assembly was insulated using hollow cylinders of compressed NaCl and wrapped in Pb foil. The

Table 1
REE-chloride and actinide components (Mix 1) used as a part of the experimental charge.

Chemical	Added (mg)
$LaCl_3$	71.48
$CeCl_3$	141.85
$PrCl_3$	16.97
YCl_3	222.34
$SmCl_3$	7.17
$EuCl_3$	7.1
$GdCl_3$	7.3
$LuCl_3$	0.93
$DyCl_3$	8.09
$UO_2Cl_2.2H_2O$	5.88
$Th(NO_3)_4$	27.7

experimental assembly is shown in Fig. 1.

The sample was pressurized to 1 GPa, which was displayed on a 20 cm Heise pressure gauge, and heated at 100 °C/min to the dwell T. The temperature was monitored using a W75Re25 and W97Re3 thermocouple wire, procured from Concept Alloys Inc. (accuracy of ±3 °C as stated by the company), encased in mullite. At the end of its dwell time, the experiment was quenched by cutting off power to the instrument. Afterward, we carefully opened the Pt capsule to collect the experimental fluid and then extracted the mineral phases. We then mounted the mineral phases on double-sided tape, which was then cast onto a 1″ epoxy disc and polished using 1 μm alumina powder followed by a colloidal solution of silica (~0.05 μm). The experimental products were imaged using a Hitachi TM4000 benchtop SEM (Scanning Electron Microscope), housed at the University of Rochester, after polishing to make sure that sizeable crystals of monazite and xenotime had crystallized. After imaging, the phases were measured using an LA-ICP-MS.

Before the main experiments (Table 2), we performed some exploratory experiments without buffering the oxygen fugacity. These were done in a simple $Ce(OH)_3$-$Y(OH)_3$-P_2O5-H_2O or a $CeCl_3$-YCl_3-P_2O_5-H_2O system (See Supplementary Information) at a suite of Ts and 0.7/1 GPa to optimize the experimental charge, capsule design, and the experimental duration. To rule out any significant instrumental errors from experimental pressure, we also performed NaCl melting experiments to calibrate the true pressure vs. nominal pressure for our piston cylinder (See Supplementary Information).

2.3. Synthetic standards

We grew monazite ($CePO_4$) and xenotime (YPO_4) in a 1 atm tube furnace (Cherniak et al., 2004) to use as matrix-matched standards for laser ablation measurements. The flux-grown monazite was used to calibrate the [Ce] in both phosphate phases, and the flux-grown xenotime was used to calibrate the [Y] in the same. Monazite and xenotime were synthesized by fluxing $CeCl_3$/YPO_4 and H_3PO_4 in Li_2CO_3 and MoO_3 in a 25 mL Pt crucible. Monazite was grown by holding the sample at ~1350 °C for 3 h, followed by cooling to 950 °C at 3°/h for a total duration of ~5 days. Similarly, xenotime was synthesized by holding the crucible at 1350 °C for 9 h and then cooling to 900 °C at the same rate. After the fluxing, the crystals (0.5–2 mm and largely inclusion-free) were extracted, cleaned in an ultra-sonic cleaner, cast onto a 1″ epoxy disc, and polished (Fig. S7).

2.4. Mass spectrometry measurements

2.4.1. Experimental products

Monazite and xenotime were analyzed with the University of Rochester Cetac (formerly Photon Machines) Analyte G2 193 nm excimer LA system coupled to an Agilent 7900 quadrupole ICP-MS. We used this setup to analyze the experimental products and NIST glass standards. The LA system has a HelEx II sample chamber where samples are transported to the ICP-MS after ablation using He as a carrier gas. Helium flows in the HelEx chamber at 0.6 L/min and in the carrier gas tube upon exiting the chamber at 0.2 L/min. Before the sample was introduced into the plasma, we also introduced Ar as a carrier gas at 1.3 L/min.

We used a sample-standard bracketing system in which the standards were flux-grown phosphates and NIST610. The latter was used to calibrate all the analytes except Ce and Y. Cerium and Y are the predominant cations in the experimental mix, and possible matrix effects are minimized for these two cations. There is a 20% difference in

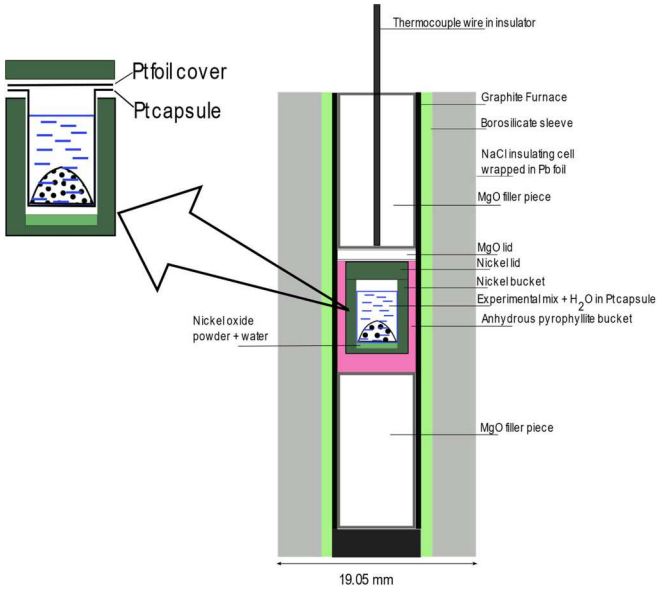

Fig. 1. Illustration of the experimental assembly used to derive the main thermometer. The assembly comprised of a graphite furnace surrounded by borosilicate glass. The whole assembly was encased in compressed NaCl. The 5 mm diameter Pt capsule was welded at the bottom and inserted into an oxidized Ni bucket, 8 mm long. The capsule had a Pt foil and oxidized Ni lid, 2 mm tall on top of it. The capsule was sealed by the Pt foil during cold pressurization. The Ni bucket was surrounded by MgO which was the pressure media. Additional details may be found in Trail et al., 2019.

Table 2
Experimental details and conditions.

Experiment name	T (°C)/P (GPa)	Experiment duration (h)	NiO added[a] (mg)	Mix 1 (mg)	H_3PO_4 (mg)	NaCl (mg)	H_2O (mg)	Fluid collected post-experiment (μL)
MXT1_4.5 N	1150/1	48	19.45	19.52	8.69	2.1	17.27	1.5
MXT1_4N	1100/1	48	18.02	18.08	8.6	5.62	27.6	1.3
MXT1_3.5 N	1050/1	48	16.68	19.27	9.97	2.52	14.33	4.25
MXT1_3N	1000/1	48	17.23	18.42	8.39	4.77	30.69	–
MXT1_2.5 N	950/1	168	19.23	19.89	9.74	1.42	49.53	4
MXT1_2N(II)	900/1	168	19.51	19.51	11.02	1.39	23.76	1
MXT1_1.5 N	850/1	336	19.23	19.57	8.84	2	29	3.25

[a] Amount of NiO added to the bottom of the Ni bucket.

concentration for Ce in xenotime and an almost 50% difference for Y in monazite if we use NIST610 instead of a matrix-matched standard (Table 3). We therefore decided to use a matrix-matched standard.

We analyzed the experimental phosphates by pulse-firing the laser at a fluence of 4.72 J/cm2 for 15 s with a pulse frequency of 10 Hz. We used a 5 μm circular spot on all experimental phosphates. Preceding the 15 s ablation period was a 20s period during which the background signal was collected and succeeding it was a 35 s period during which we allowed the system to flush with carrier gas in preparation for the next analysis. We analyzed ^{140}Ce, ^{89}Y, ^{139}La, ^{141}Pr, ^{147}Sm, ^{153}Eu, ^{155}Gd, ^{163}Dy, ^{175}Lu, ^{232}Th, ^{238}U and ^{31}P. Phosphorus-31 was used as the internal standard, while the rest of the REEs were used to calibrate the thermometer. For the raw data calibration, we used the Iolite 3.32 software package (Paton et al., 2011).

We were able to extract and analyze (Details in Supplementary information) the experimental fluid of 13 experiments (including those discussed in the main text and the supplementary information) after they were completed (Table ST4).

3. Results

3.1. Experimental data

The phosphates are euhedral to subhedral and range from <1 to 10 μm, depending on the temperature and the duration of the experiment (Fig. 2). For the lowest T experiment (850 °C) monazite grains were approximately 10 μm, whereas the xenotime were ~ 1 μm. In the case of the latter, they were not large enough to analyze and no chemical data are reported for xenotime from this experiment. Table 4 presents the average REE concentrations of the monazite and the xenotime for the experiments. Since we have used a small spot size and our mounts have clusters of both phosphates, we scrutinized the data for anomalies. We did notice some inclusions of xenotime in monazite and vice versa in some of the larger grains and thus data that are clean with uniform Ce and Y signals throughout the laser ablation integration were used to derive elemental concentrations. Approximately 90% of the data collected met these criteria.

The respective [Y] and [Ce] of monazite and xenotime decrease with temperature. This trend is expected if we write the following exchange reactions:

$$YPO_4^{Xnt} \leftrightarrow YPO_4^{Mzt} \tag{6a}$$

$$CePO_4^{Mzt} \leftrightarrow CePO_4^{Xnt} \tag{6b}$$

and the respective derivative partitioning relationships with T:

$$\frac{-\Delta G^0_Y}{2.303RT} - log\ \gamma_Y = log\ D_Y^{Mzt/Xnt} \tag{7a}$$

$$\frac{-\Delta G^0_{Ce}}{2.303RT} - log\ \gamma_{Ce} = log\ D_{Ce}^{Xnt/Mzt} \tag{7b}$$

Where $\Delta G^0_{Y/Ce}$ is the change in Gibbs free energy in the standard state for Eqs. (6a)/(6b), and R is gas constant in J/(mol × K).

The monazite have [Y] that range from 26.60 ± 1.54 at.% at 1150 °C to 16.13 ± 1.62 at. % at 850 °C (2 s.e.). Xenotime have [Ce] of 0.66 ± 0.07 at.% 1150 °C to 0.46 ± 0.02 at.% at 900 °C.

Along with the composite correlations involving multiple REEs, we also correlated the partitioning of each REE between monazite and xenotime with 10^4/T. If the compositions of two phosphate phases in an experiment are in equilibrium, the ΔG^0 of each of these partitioning reactions may be related to the partition coefficient through:

$$\frac{-\Delta G^0}{2.303RT} - log\ \gamma = log\ D^{Mzt/Xnt} \tag{8}$$

Eq. (8) is a linear correlation between Log D vs 1/T(K). Therefore, $\frac{-\Delta G^0}{2.303R}$ is the slope of the correlation and thus ΔG^0 can be calculated using the following formula:

$$\Delta G^0 = -m \times 2.303 \times R \tag{9}$$

Where m = experimentally obtained slope of the regression line of each REE.

We also observed that significant quantities of Th and U (Table 4) were incorporated into both phosphate phases. While this is commonly observed assuming the two proposed substitution mechanisms;

$$REE^{3+} + P^{5+} \rightarrow Th/U^{4+} + Si^{4+}\ (Huttonite) \tag{10a}$$

$$2\ REE^{3+} \rightarrow Ca^{2+} + Th^{4+}\ (Cheralite), \tag{10b}$$

these require the presence of Ca and/or Si in the system which are absent in our experimental charge. Thus, future studies could be conducted to explore the precise nature of the substitution mechanism for both actinides.

4. Discussion

4.1. Thermometry model

The monazite-xenotime partition coefficients of individual REEs + Y are also shown against 10^4/T (Fig. 3A). These correlations show that the LREEs (La, Ce, Pr, Sm and Eu) prefer the monazite structure $\left((D_{LREE})^{Mzt/Xnt} > 1\right)$ while the HREEs (Dy and Lu) and Y prefer the xenotime structure $\left((D_{Y,HREE})^{Mzt/Xnt} < 1\right)$, as observed by Franz et al. (1996). Gadolinium prefers the monazite structure at our experimental Ts $\left((D_{Gd})^{Mzt/Xnt} > 1\right)$. However, the Gd regression line has a negative slope. This implies that at lower Ts (~700 °C and below), the $(D_{Gd})^{Mzt/Xnt}$ will be <1 and Gd is predicted to prefer the xenotime structure. This experimental prediction is observed in nature (Franz et al., 1996).

Of all the REEs shown in Fig. 3A, we find that Y, La, Ce and Pr regressions have the greatest sensitivities and the greatest R^2 values and so we combined the data for these elements to formulate a calibration in the form of Eq. (5). Fig. 4 shows the relation between $log\left(\frac{\prod X_{Xnt}^{LREE} \times X_{Mzt}^{Y}}{\prod X_{Mzt}^{LREE} \times X_{Mzt}^{Y}}\right)$ and 10^4/T (K). Where LREE = La, Ce and Pr.

The calibration has the equation:

$$log\left(\frac{\prod X_{Xnt}^{LREE} \times X_{Mzt}^{Y}}{\prod X_{Mzt}^{LREE} \times X_{Mzt}^{Y}}\right) = \frac{(-6714 \pm 2264)}{T\ (K)} - (0.79 \pm 1.76)\ \left(R^2 = 0.9\right) \tag{11}$$

Table 5 lists the data that were used to create the calibration of Fig. 4. The concentration values (at. %) used to derive the $log\left(\frac{\prod X_{Xnt}^{LREE} \times \prod X_{Mzt}^{Y}}{\prod X_{Mzt}^{LREE} \times \prod X_{Xnt}^{Y}}\right)$ values were obtained from Table 4. For example, for the experiment done at 1150 °C,

$$\prod X_{Xnt}^{LREE} \times X_{Mzt}^{Y} = ([La] \times [Ce] \times [Pr]\ in\ Xnt) \times ([Y] n\ Mzt)$$

$$\therefore (0.28 \pm 0.03) \times (0.65 \pm 0.03) \times (0.20 \pm 0.02\ ) \times (26.60 \pm 1.54)$$
$$= 1.00 \pm 0.18$$

Table 3
Differences in reported concentrations for phosphates grown at 1100 °C based on calibration standards.

	Y in monazite (wt%)			Ce in xenotime (wt%)		
Matrix matched std.	0.63	±	0.02	14.40	±	0.71
NIST610 calibrated	0.93	±	0.04	17.65	±	2.15

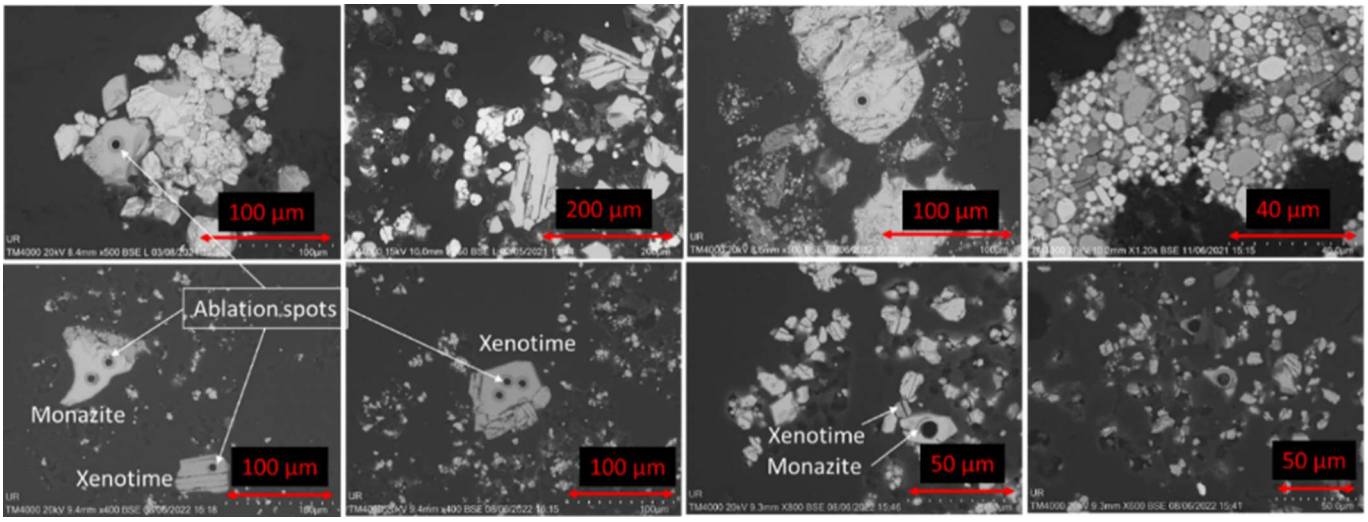

Fig. 2. Representative Back Scattered Electron (BSE) images of experimental monazite (light gray phase) and xenotime (dark gray phase) and the large range of crystal sizes encountered in our experimental products. Also shown are examples of ablation spots (5 µm).

Similarly,

$$\prod X_{Mzt}^{LREE} \times X_{Xnt}^{Y} = (25.60 \pm 5.22) \times 10^4$$

Thus,

$$log\left(\frac{\prod X_{Xnt}^{LREE} \times X_{Mzt}^{Y}}{\prod X_{Mzt}^{LREE} \times X_{Xnt}^{Y}}\right) = log\left(\frac{1.00 \pm 0.18}{(25.60 \pm 5.22) \times 10^4}\right) = -5.41 \pm 0.12.$$

While most of these correlations are quite sensitive to T, if we can create subsequent calibrations using ratios of element pairs with the greatest difference in regression line slopes, which are a function of ΔG^0, their sensitivity to T will be magnified. For example, the $log(D_{La})^{Mzt/Xnt}$ and $log(D_Y)^{Mzt/Xnt}$ regressions have slopes of 0.25 and − 0.12 respectively but the log $(D_{La}/D_Y)^{Mzt/Xnt}$ vs. 10^4/T regression has a slope of 0.37 which has a greater absolute value and therefore implies greater sensitivity to changes in T. Fig. 6 presents of some derivative calibrations like the log $(D_{Ce}/D_Y)^{Mzt/Xnt}$ vs. 10^4/T regression. The regression lines involving the elements with the greatest difference in ΔG^0 (La/Y, Ce/Y, La/Gd, etc.) have greater slopes implying greater sensitivity to T compared to the elements with smaller differences in ΔG^0 (Ce/Pr). This is shown in Fig. 5.

The regression lines of Figs. 3A and 5 have the general form

$$log\ [D_{Element}]^{Mzt/Xnt} = \frac{10^4 \times (A \pm \sigma_A)}{T\ (K)} + (B \pm \sigma_B). \quad (12)$$

where A and B are experimentally derived parameters and σ is the 2 s.e. associated with them. Table 6 shows the values of the experimentally derived parameters for each of the calibrations.

4.2. Natural monazite and xenotime of the Northern Highland Terrane

With the partitioning systematics explored, we have applied our thermometer to published monazite and xenotime data from quartzo-feldspathic psammites and garnet-bearing pelites from the Naver nappe in the Northern Highlands Terrane (Mako et al., 2019; Ashley et al., 2015), metamorphosed to the amphibolite facies.

Eleven hand samples were presented in Mako et al., 2019 (NT-01 through NT-11). Based on the petrography and Zr-in-titanite thermometry from one of the samples (NT-02), the Naver nappe experienced upper amphibolite to granulite facies metamorphism (600–739 °C; 6–9 kbar (Mako et al., 2019)). They also used the monazite-xenotime thermometers of Heinrich et al., 1997 and Pyle et al., 2001 to report equilibrium Ts of 393–675 °C and 510–600 °C respectively. While the Gratz and Heinrich, 1997 and Seydoux-Guillaume et al., 2002 thermometers return Ts of 625–790 °C for most of the samples. Finally, the Gratz and Heinrich, 1998 thermometer based on Gd partitioning provides estimates of 910–1150 °C. Mako et al., 2019 prefer the T estimates of the Heinrich et al., 1997 thermometer (393–675 °C) since it is most comparable to the petrographic T estimates. While the T estimates of around 600–675 °C corroborate the petrographic observations, at these Ts, the samples in question ought to have evidence of partial melting that Mako et al., 2019 were unable to detect.

Of the eleven samples, one of them (NT-02) is a titanite-bearing calcsilicate and no phosphate data has been reported for it. From the remaining ten, we have eliminated two samples (NT-01 and NT-04) since the monazite show strong zoning patterns indicative of an igneous origin and therefore equilibrium with xenotime could not be evaluated by Mako et al., 2019. Two more samples have been excluded (NT-07 and NT-09) since they do not contain any xenotime and the Ts reported by Mako et al., 2019 are minimum T estimates. Another sample also does not contain xenotime (NT-10) but the monazite in this sample are texturally and compositionally similar to those in a xenotime-bearing sample (NT-11) and are thus considered to be in equilibrium with xenotime by Mako et al., 2019. The analyses that had percentage discordance $\left(100 - \left(\left(\frac{^{206}/_{238}\ Age}{^{207}/_{235}\ Age}\right)*100\right)\right)$ between −10 and 10 were selected for discussion. Of all of the samples, that have both phosphate phases, monazite and xenotime are broadly similar in age. Our selected samples have average ^{207}Pb-^{206}Pb ages between 412 ± 26 and 440 ± 24 Ma (average of the entire monazite and xenotime population from each sample; errors are 2 s.d.). These similar ages suggest that our selected samples experienced the same metamorphic event and that we have quantified the same. There were some analyses (8 out of 310) that were within our discordance limits but had high ages (650–970 Ma); these were discarded.

4.2.1. Evaluation of chemical equilibrium

Before we applied our thermometers, we performed a test to assess whether the REE contents of co-existing natural phosphates are consistent with chemical equilibrium. First, we derive two empirical thermometers using our experimental data: one that relates log [Y] in monazite (at. %) vs. 10^4/T (K) and another that relates log [La*Ce*Pr] in xenotime (at. %) vs. 10^4/T (K). They are:

$$log[Y]^{Mzt} = \frac{(-1136 \pm 240)}{T\ (K)} + (2.21 \pm 0.10)\ (R^2 = 0.95) \quad (13)$$

Table 4
Average REE and actinide contents (At. %) of experimental monazite and xenotime.

Experiment name	Phase	T(°C)/P (GPa)	Duration of Expt. (h)	n	[Y] (± 2 s.e.) (%)	[La] (± 2 s.e.) (%)	[Ce] (± 2 s.e.) (%)	[Pr] (± 2 s.e.) (%)	[Sm] (± 2 s.e.) (%)	[Eu] (± 2 s.e.) (%)	[Gd] (± 2 s.e.) (%)
MXT1_4.5 N		1150/1	48	14	26.60 ± 1.54	23.11 ± 3.31	37.20 ± 3.62	3.17 ± 0.35	1.38 ± 0.16	1.30 ± 0.16	1.41 0.09
MXT1_4N		1100/1	48	6	24.09 ± 2.93	23.50 ± 5.59	39.25 ± 10.71	3.26 ± 0.82	1.26 ± 0.35	1.11 ± 0.28	1.18 ± 0.34
MXT1_3.5 N		1050/1	48	10	22.09 ± 1.84	23.93 ± 1.92	41.57 ± 3.26	3.40 ± 0.30	1.45 ± 0.16	1.30 ± 0.15	1.16 ± 0.11
MXT1_3N	**Monazite**	1000/1	48	19	19.00 ± 1.39	24.03 ± 1.94	43.51 ± 3.57	3.40 ± 0.31	1.45 ± 0.12	1.32 ± 0.09	1.13 ± 0.08
MXT1_2.5 N		950/1	168	8	20.10 ± 2.29	24.58 ± 3.85	41.68 ± 4.14	3.72 ± 0.40	1.54 ± 0.18	1.35 ± 0.12	1.06 ± 0.09
MXT1_2N(II)		900/1	168	5	17.15 ± 1.51	23.70 ± 3.42	46.46 ± 5.25	3.43 ± 0.47	1.43 ± 0.18	1.28 ± 0.14	1.08 ± 0.12
MXT1_1.5 N		850/1	336	12	16.13 ± 1.62	26.25 ± 2.65	52.83 ± 4.90	3.73 ± 0.38	1.50 ± 0.15	1.38 ± 0.13	1.06 ± 0.08
MXT1_4.5 N		1150/1	48	6	93.54 ± 0.27	0.28 ± 0.03	0.65 ± 0.03	0.20 ± 0.02	0.50 ± 0.05	0.68 ± 0.08	0.96 ± 0.08
MXT1_4N		1100/1	48	19	94.49 ± 7.89	0.20 ± 0.01	0.65 ± 0.04	0.16 ± 0.01	0.40 ± 0.03	0.55 ± 0.04	0.78 ± 0.06
MXT1_3.5 N		1050/1	48	14	94.45 ± 9.79	0.23 ± 0.02	0.68 ± 0.06	0.14 ± 0.01	0.42 ± 0.05	0.62 ± 0.07	0.87 ± 0.11
MXT1_3N		1000/1	48	10	93.52 ± 13.39	0.13 ± 0.02	0.56 ± 0.05	0.13 ± 0.02	0.41 ± 0.06	0.58 ± 0.08	0.82 ± 0.12
MXT1_2.5 N		950/1	168	10	94.58 ± 6.55	0.17 ± 0.03	0.61 ± 0.07	0.13 ± 0.01	0.41 ± 0.03	0.50 ± 0.10	0.77 ± 0.23
MXT1_2N(II)		900/1	168	6	93.12 ± 3.97	0.11 ± 0.01	0.46 ± 0.02	0.125 ± 0.006	0.44 ± 0.02	0.63 ± 0.03	0.89 ± 0.04
MXT1_1.5 N	**Xenotime**	850/1	336	–	– – –	– – –	– – –	– – –	– – –	– – –	– – –

Experiment name	Phase	T(°C)/P(GPa)	Duration of Expt. (h)	n	[Eu] (± 2 s.e.) (%)	[Gd] (± 2 s.e.) (%)	[Dy] (± 2 s.e.) (%)	[Lu] (± 2 s.e.) (%)	[Th] (± 2 s.e.) (%)	[U] (± 2 s.e.) (%)
MXT1_4.5 N		1150/1	48	14	1.3 ± 0.16	1.41 ± 0.09	1.14 ± 0.11	0.05 ± 0.01	4.28 ± 0.58	0.39 ± 0.06
MXT1_4N		1100/1	48	6	1.11 ± 0.28	1.18 ± 0.34	1.02 ± 0.22	0.04 ± 0.01	4.95 ± 0.98	0.35 ± 0.08
MXT1_3.5 N		1050/1	48	10	1.3 ± 0.15	1.16 ± 0.11	0.99 ± 0.05	0.04 ± 0.01	3.71 ± 0.51	0.36 ± 0.05
MXT1_3N		1000/1	48	19	1.32 ± 0.09	1.13 ± 0.08	0.94 ± 0.08	0.023 ± 0.002	4.23 ± 0.32	0.97 ± 0.11
MXT1_2.5 N		950/1	168	8	1.32 ± 0.12	1.03 ± 0.09	0.91 ± 0.09	0.033 ± 0.004	4.21 ± 0.57	0.66 ± 0.05
MXT1_2N(II)		900/1	168	5	1.28 ± 0.14	1.08 ± 0.12	0.9 ± 0.09	0.03 ± 0.01	4.19 ± 0.6	0.34 ± 0.05
MXT1_1.5 N	**Monazite**	850/1	336	12	1.38 ± 0.13	1.06 ± 0.08	0.87 ± 0.07	0.02 ± 0.01	3.85 ± 0.43	0.42 ± 0.03
MXT1_4.5 N		1150/1	48	6	0.68 ± 0.08	0.96 ± 0.08	2.5 ± 0.25	0.56 ± 0.07	0.06 ± 0.01	0.06 ± 0.01
MXT1_4N		1100/1	48	19	0.55 ± 0.04	0.78 ± 0.06	1.99 ± 0.16	0.37 ± 0.03	0.2 ± 0.02	0.19 ± 0.03
MXT1_3.5 N		1050/1	48	14	0.62 ± 0.07	0.87 ± 0.11	2.11 ± 0.23	0.38 ± 0.05	0.07 ± 0.01	0.05 ± 0.01
MXT1_3N		1000/1	48	10	0.58 ± 0.08	0.82 ± 0.12	2.16 ± 0.32	0.37 ± 0.05	0.45 ± 0.06	0.88 ± 0.16
MXT1_2.5 N		950/1	168	10	0.53 ± 0.05	0.84 ± 0.07	2.2 ± 0.21	0.36 ± 0.03	0.07 ± 0.01	0.11 ± 0.02
MXT1_2N(II)		900/1	168	6	0.63 ± 0.03	0.89 ± 0.04	2.22 ± 0.09	0.33 ± 0.01	0.89 ± 0.05	0.78 ± 0.06
MXT1_1.5 N	**Xenotime**	850/1	336	–	– – –	– – –	– – –	– – –	– – –	– – –

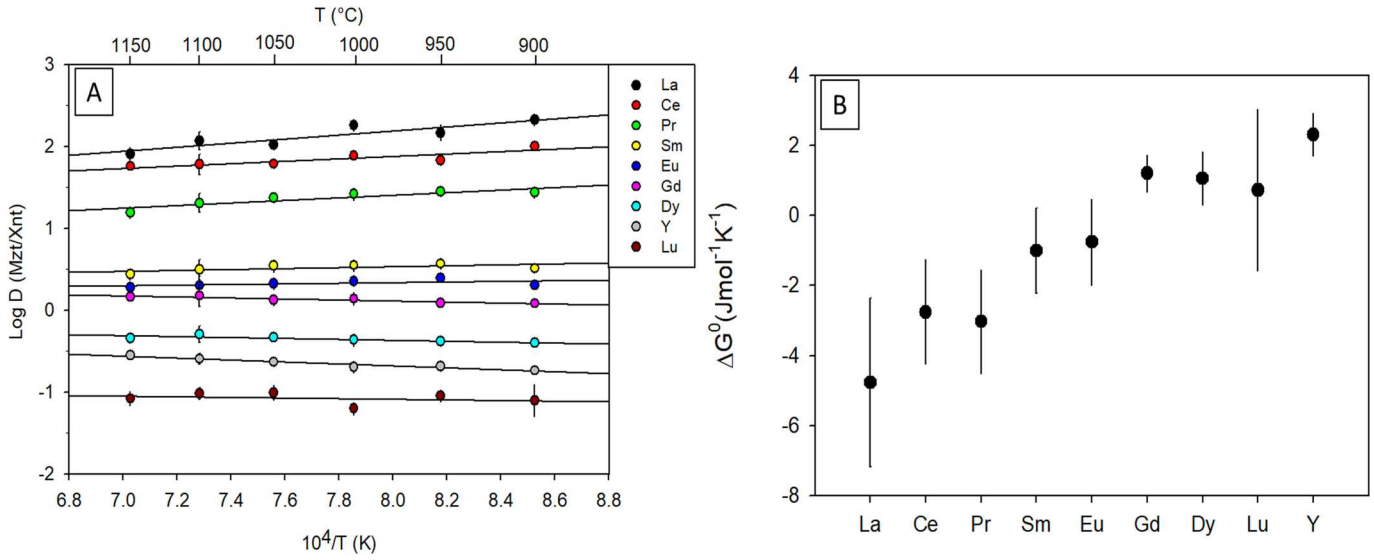

Fig. 3. A Change in Monazite/Xenotime partition coefficient with 10^4/T for each REE and Y. These regression lines follow the functional form of Eq. (6) and may in principle be used individually as thermometers. However, the T sensitivities of Y, La, Ce and Pr are greater than the rest of the REEs (Sm, Eu, Dy and Lu) which have near-zero slopes. This implies that the standard-state enthalpy change (ΔH^0) for the rest of the REEs is also near-zero. Thus, Y, La, Ce, Pr and Gd have been used to create our main calibration (Eq. (10)). B: $\Delta G^0$of the REE exchange reactions derived from the regression lines of Fig. 3A. These values have been derived using Eq. (9).

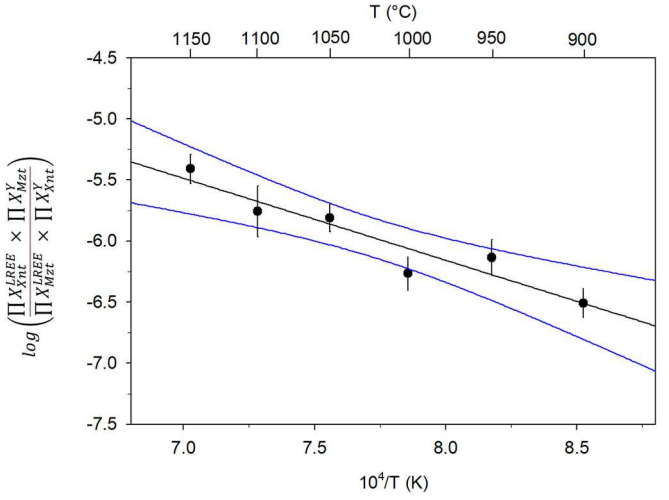

Fig. 4. Primary thermometer derived using the elements Y, La, Ce, Pr and Gd. The blue curves are the 95% confidence limit. Errors are 2 s.e. Data from the experiment at 850 °C is not shown here since xenotime grains from this experiment could not be analyzed. (For interpretation of the references to colour in this figure legend, the reader is referred to the web version of this article.)

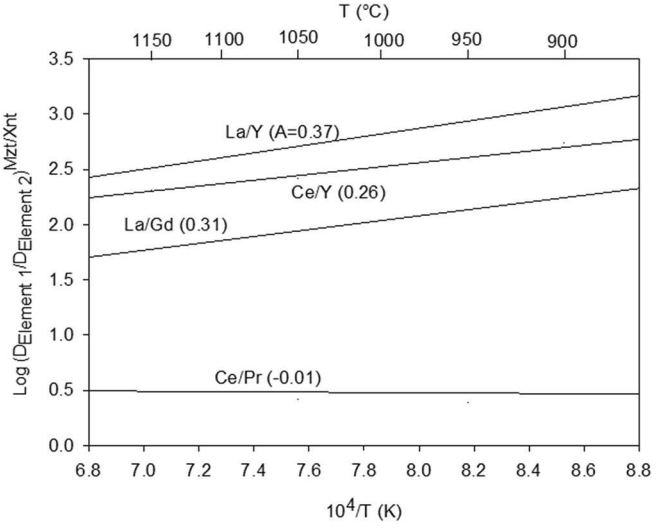

Fig. 5. Derivative thermometers from partition coefficients calculated for individual elements. Note the greater T sensitivity for calibrations involving elements with greater differences in ΔG^0 values (Ce/Y, La/Dy, etc.).

Table 5
Products of concentrations used to derive the calibration of Fig. 4. All errors are 2 s.e.

T (°C)	10^4/T(K)	$\prod X_{Xnt}^{LREE} \times \prod X_{Mzt}^{Y}$			$\prod X_{Mzt}^{LREE} \times \prod X_{Xnt}^{Y}$			$log\left(\frac{\prod X_{Xnt}^{LREE} \times \prod X_{Mzt}^{Y}}{\prod X_{Mzt}^{LREE} \times \prod X_{Xnt}^{Y}}\right)$		
1150	7.03	9.96E-01	±	1.81E-01	2.55E+05	±	5.22E+04	−5.41	±	0.12
1100	7.28	4.97E-01	±	8.64E-02	2.84E+05	±	1.27E+05	−5.76	±	0.21
1050	7.56	4.92E-01	±	9.51E-02	3.20E+05	±	5.66E+04	−5.81	±	0.11
1000	7.86	1.80E-01	±	4.31E-02	3.33E+05	±	6.82E+04	−6.27	±	0.14
950	8.18	2.60E-01	±	6.62E-02	3.54E+05	±	7.64E+04	−6.13	±	0.15
900	8.53	1.10E-01	±	1.56E-02	3.52E+05	±	8.21E+04	−6.51	±	0.12

Table 6
Experimental parameters derived for each of the individual Y + REE calibrations.

Element	A (± 2 s.e.)			B (± 2 s.e.)			R^2
Y[A]	−0.121	±	0.031	0.286	±	0.244	0.94
La[B]	0.249	±	0.125	0.200	±	0.972	0.80
Ce[C]	0.144	±	0.078	0.730	±	0.604	0.77
Pr[D]	0.158	±	0.077	0.141	±	0.601	0.81
Sm	0.052	±	0.064	0.114	±	0.493	0.40
Eu	0.039	±	0.064	0.022	±	0.496	0.27
Gd	−0.063	±	0.028	0.616	±	0.216	0.84
Dy	−0.055	±	0.040	0.078	±	0.307	0.66
Lu	−0.038	±	0.120	−0.783	±	0.931	0.09
La/Y	0.370	±	0.151	−0.086		1.169	0.86
Ce/Y	0.264	±	0.094	0.444	±	0.726	0.89
La/Gd	0.312	±	0.099	−0.416	±	0.766	0.91
Ce/Pr	−0.014	±	0.133	0.589	±	1.033	0.01

A-D: Eqs. discussed in section 4.2.

$$log[La \times Ce \times Pr]^{Xnt} = \frac{(-4554 \pm 1948)}{T\ (K)} + (1.71 \pm 0.76)\ \left(R^2 = 0.85\right) \quad (14)$$

If the natural monazite and xenotime crystallized in chemical equilibrium with each other, then the calibrations shown above should return similar T estimates from coeval phosphates. The reader should be aware that we do not claim these estimates to be accurate metamorphic Ts beacause Eqs. (13) and (14) are empirical calibrations and not based in thermodynamic theory.

We performed these calcuations using the average [REE] values of our filtered analyses. The calculated Ts of three of the selected samples (NT-05, NT-10 and NT-11), when Eqs. (13) and (14) are applied, lie close to the 1:1 line within analytical uncertainty (Discordance between 2 and 5%; $Discordance = \left(1 - \frac{Xnt\ T\ est.}{Mzt\ T\ est.}\right) \times 100$) (Fig. 6). The three other samples (NT-03, NT-06 and NT-08) return similar T estimates (Discordance between −16 and 16%) but are not on the 1:1 line. Even though not all the samples lie close to the 1:1 line, they all fall, within uncertainity, within the same metamorphic facies field. This reflects phosphate growth under similar metamorphic conditions. This test, along with the textural and geochronological observations made by Mako et al., 2019 may be used to test equilibrium between coexisting or coeval phases.

We would like to point out that T is one intensive variable out of others (P, fO_2, etc) that control chemical equilibrium and until this system is exhaustively quantified, we are assuming that the phosphates record the same metamorphic conditions.

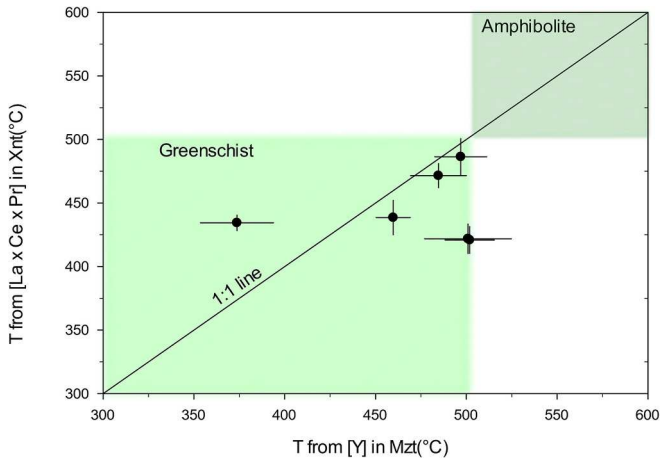

Fig. 6. Comparison of temperature estimates (± 2 s.e.) using Eqs. (13) and (14). The T estimates are like each other within analytical uncertainty implying that the natural phosphates experienced similar metamorphic Ts.

4.2.2. Monazite-xenotime thermometry

We applied our main thermometer (Eq. (11)) as well as four single-element thermometers (Y, La, Ce and Pr; Eqs. A-D (Table 6)) that have the highest sensitivity and R^2 values. We averaged the Y, La, Ce and Pr concentrations of the monazite and xenotime populations of each of the six samples discussed in this study. We then used these averaged values to calculate $log\left(\frac{\prod X_{Xnt}^{LREE} \times X_{Mzt}^{Y}}{\prod X_{Mzt}^{LREE} \times X_{Xnt}^{Y}}\right)$ or $log\left(D_{Element}^{Mzt/Xnt}\right)$ which were subsequently used to calculate T (Fig. 7). The T estimates are similar and lie in the upper greenschist – lower amphibolite T range. The main thermometer (Eq. (11)) returns T estimates between 471 and 540 °C while the single element thermometers (Eqs. A-D) return T estimates similar to each other (Fig. 7). The Ce thermometer returns T estimates (420–496 °C) that are slightly lower than the rest but still within the upper greenschist – lower amphibolite T range. The T estimates derived from Eq. (11) and A-D are offset from the previous T estimates derived using the calibration of Heinrich et al., 1997. Note that the Heinrich et al., 1997 calibration was empirical and natural samples used might not have the intensive variables (P, T, fO_2, etc.) that affect elemental partitioning properly constrained. This could compound the sources of error from the unconstrained empirical calibration as well as the natural dataset leading to greater inaccuracies in the published T estimates compared to our T estimates. Moreover, Heinrich et al., 1997 also used phosphates from greenschists to granulites which imply changing P and T, while our experiments were performed at a constant P of 10 kbar. This means that the two calibrations, which were implemented with different stragegies, are not directly comparable. Mako et al., 2019 report that the phosphates were in equilibrium during the retrograde arm of the metamorphic path. This is based on geochronology of the phosphates discussed here, which have a lower age (~420 Ma) than the Northern Highlands Terrane (980–870 Ma). So, our T estimates may be recording the retrograde T rather than the peak T conditions.

5. Summary and outlook

We have derived calibrations for T-dependent, Y + REE (at. %) partitioning between monazite and xenotime for a system, and we have

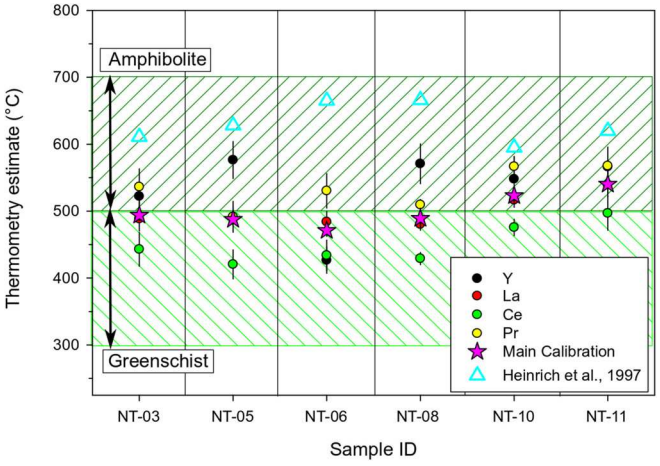

Fig. 7. Temperature estimates based on our monazite-xenotime thermometers (circles and stars) as well as those reported by Mako et al., 2019 using the Heinrich et al., 1997 thermometer (cyan triangles). Our estimates were derived using Eq. (11) (pink stars) and Eqs. A-E (circles; Table 6). The shaded regions are the T range of the amphibolite and greenschist facies. Most of our T estimates lie within the upper-greenschist to amphibolite field in accordance with the petrographic observations. Error bars are 2 s.e. that have been propagated from errors on the natural phosphate measurements since it is the major source of the error (Calculations in Supplementary file). (For interpretation of the references to colour in this figure legend, the reader is referred to the web version of this article.)

presented evidence consistant with the interpretation that the experimental phases crystallized at or close to equiliburm. We have created a basis for a robust thermometer in a Y-REE-U-Th-NaCl bearing water saturated system, broadly similar to a natural metamorphic system and by employing precise in-situ analytical techniques.

The most important aspect of the thermometers presented here is their versatility. Since the system of interest is complex, involving multiple cation exchange reactions, multiple thermometers may be derived by combining various REEs (Eq. (10)) depending on the demands of the natural system or the data available. Finally, one could also use single-element thermometers (Table 6) in addition to the main combined calibration (Eq. (10)).

We were able to capitalize on the versatility of our thermometer when applying them to phosphates from the Northern Highland Terrane in Scotland that were analyzed by Mako et al., 2019. We also generated single element thermometers by calibrating monazite-xenotime partition coefficients for REEs. After an initial check for chemical equilibrium, when we applied our thermometers (Eqs. (11) and Eqs. A-D (Table 6)) to natural data, we found that the metamorphic Ts are between 421 and 576 °C, depending on the sample and the calibration used, which is in the upper greenschist – lower amphibolite facies region which might imply that the phosphates are recording Ts during the retrograde arm of the P-T-t path.

In conclusion, until now only a few mineral phases (zircon, garnet, rutile, etc.) have proved to be reliable target minerals for simultaneous thermobarometry and geochronology, and this study presents a monazite-xenotime thermometer, that builds on previous exploratory attempts at quantifying this system, using more advanced in-situ measurement techniques and experimental charges that more closely mimic natural metamorphic systems. We have also explored the effects of P and fO_2 on the REE partitioning (Supplementary information) and future studies should be undertaken to quantify the effect these intensive variables have on the system.

CRediT authorship contribution statement

Wriju Chowdhury: Data curation, Formal analysis, Investigation, Methodology, Validation, Visualization, Writing – original draft, Writing – review & editing. **Dustin Trail:** Conceptualization, Project administration, Supervision, Validation, Writing – review & editing.

Declaration of competing interest

The authors declare that they have no known financial or personal competing interests.

Data availability

All processed data is presented in the manuscript.

Acknowledgements

This work has been funded by the National Science Foundation (EAR-1751903, & EAR-2327940). Special thanks go out to Dr. Calvin Mako of The Arizona Geological Survey whose comments and advice have greatly improved the manuscript. We also thank psudoanonymous reviewer “MJJ” and an anonymous reviewer for their time and comments that have been incorporated into the manuscript.

Appendix A. Supplementary data

Supplementary data to this article can be found online at https://doi.org/10.1016/j.chemgeo.2024.121939.

References

Andrehs, G., Heinrich, W., 1998. Experimental determination of REE distributions between monazite and xenotime: potential for temperature-calibrated geochronology. Chem. Geol. 149, 83–96.
Ashley, K.T., Thigpen, J.R., Law, R.D., 2015. Prograde evolution of the Scottish Caledonides and tectonic implications. Lithos 224-225, 160–178.
Cherniak, D.J., Pyle, J., Rakovan, J., 2004. Synthesis of REE and Y phosphates by Pb-free flux methods and their utilization as standards for electron microprobe analysis and in design of monazite chemical U-Th-Pb dating protocol. Am. Mineral. 89 (10), 1533–1539.
Elkins, L.T., Grove, T.L., 1990. Ternary feldspar experiments and thermodynamic models. Am. Mineral. 75, 544–559.
Ferry, J.M., Spear, F.S., 1978. Experimental calibration of partitioning of Fe and Mg between Biotite and Garnet. Contrib. Mineral. Petrol. 66, 113–117.
Ferry, J.M., Watson, E.B., 2007. New thermodynamic models and revised calibrations for the Ti-in-zircon and Zr-in-rutile thermometers. Contrib. Mineral. Petrol. 154, 429–437.
Fletcher, I.R., McNaughton, N.J., Aleinikoff, J.A., Rasmussen, B., Kamo, S.L., 2004. Improved calibration procedures and new standards for U-Pb and Th-Pb dating of Phanerozoic xenotime by ion microprobe. Chem. Geol. 209, 295–314.
Franz, G., Andrehs, G., Rhede, D., 1996. Crystal chemistry of monazite and xenotime from Saxothuringian-Moldanubian metapelites, NE Bavaria, Germany. Eur. J. Mineral. 8, 1097–1118.
Ghiorso, M.S., Sack, R.O., 1991. Fe-Ti oxide geothermometry - thermodynamic formulation and the estimation of intensive variables in silicic magmas. Contrib. Mineral. Petrol. 108, 485–510.
Graham, C.M., Powell, R., 1984. A garnet hornblende geothermometer - calibration, testing, and application to the pelona schist, Southern-California. J. Metamorph. Geol. 2, 13–31.
Gratz, R., Heinrich, W., 1997. Monazite-xenotime thermobarometry: Experimental calibration of the miscibility gap in the binary system CePO4-YPO4. Am. Mineral. 82, 772–780.
Gratz, R., Heinrich, W., 1998. Monazite-xenotime thermometry. III. Experimental calibration of the partitioning of gadolinium between monazite and xenotime. Eur. J. Mineral. 10, 579–588.
Harrison, T.M., Catlos, E.J., Montel, J.M., 2002. U-Th-Pb dating of phosphate minerals. Phosphates 48, 523–558.
Heinrich, W., Andrehs, G., Franz, G., 1997. Monazite-xenotime miscibility gap thermometry. 1. An empirical calibration. J. Metamorph. Geol. 15, 3–16.
Janots, E., Engi, M., Berger, A., Allaz, J., Schwarz, J.O., Spandler, C., 2008. Prograde metamorphic sequence of REE minerals in pelitic rocks of the Central Alps: implications for allanite-monazite-xenotime phase relations from 250 to 610 degrees C. J. Metamorph. Geol. 26, 509–526.
Kohn, M.J., Vervoort, J.D., 2008. U-Th-Pb dating of monazite by single-collector ICP-MS: pitfalls and potential. Geochem. Geophys. Geosyst. 9.
Kohn, M.J., Engi, M., Lanari, P., 2017. Petrochronology: methods and application. Rev. Mineral. Geochem. 83 (1), 1–575.
Laurent, A.T., Duchene, S., Bingen, B., Bosse, V., Seydoux-Guillaume, A.M., 2018. Two successive phases of ultrahigh temperature metamorphism in Rogaland, S. Norway: evidence from Y-in-monazite thermometry. J. Metamorph. Geol. 36 (8), 1009–1037.
Mako, C.A., et al., 2019. Thermal evolution of the Scandian hinterland, Naver nappe, northern Scotland. J. Geol. Soc. Lond. 176 (4), 669–688.
Mako, C.A., Caddick, M.J., Law, R.D., Thigpen, J.R., 2024. Monazite–xenotime thermometry: a review of best practices and an example from the Caledonides of northern Scotland. Geol. Soc. Lond., Spec. Publ. 537 (1) (SP537–2022-246).
Mogilevsky, P., 2007. On the miscibility gap in monazite-xenotime systems. Phys. Chem. Miner. 34, 201–214.
O’Neill, H.S., Pownceby, M.I., 1993. Thermodynamic data from redox reactions at high-temperatures. 1. An experimental and theoretical assessment of the electrochemical method using stabilized zirconia electrolytes, with revised values for the Fe- Feo, Co-Coo, Ni-Nio and Cu-Cu2o oxygen buffers, and new data for the W-Wo2 buffer. Contrib. Mineral. Petr. 114, 296–314.
Paton, C., Hellstrom, J., Paul, B., Woodhead, J., Hergt, J., 2011. Iolite: Freeware for the visualisation and processing of mass spectrometric data. J. Anal. Atom. Spectrom. 26, 2508–2518.
Pyle, J.M., Spear, F.S., Rudnick, R.L., McDonough, W.F., 2001. Monazite-xenotime-garnet equilibrium in metapelites and a new monazite-garnet thermometer. J. Petrol. 42, 2083–2107.
Rasmussen, B., Fletcher, I.R., Muhling, J.R., 2011a. Response of xenotime to prograde metamorphism. Contrib. Mineral. Petrol. 162, 1259–1277.
Rasmussen, B., Fletcher, I.R., Muhling, J.R., Gregory, C.J., Wilde, S.A., 2011b. Metamorphic replacement of mineral inclusions in detrital zircon from Jack Hills, Australia: Implications for the Hadean Earth. Geology 39, 1143–1146.
Rauchenstein-Martinek, K., Wagner, T., Wälle, M., Heinrich, C.A., Arlt, T., 2016. Chemical evolution of metamorphic fluids in the Central Alps, Switzerland: insight from LA-ICPMS analysis of fluid inclusions. Geofluids 16 (5), 877–908.
Seydoux-Guillaume, A.M., Wirth, R., Heinrich, W., Montel, J.M., 2002. Experimental determination of Thorium partitioning between monazite and xenotime using analytical electron microscopy and X-ray diffraction Rietveld analysis. Eur. J. Mineral. 14, 869–878.
Shrestha, S., Larson, K.P., Duesterhoeft, E., Soret, M., Cottle, J.M., 2019. Thermodynamic modelling of phosphate minerals and its implications for the development of P-T-t histories: a case study in garnet - monazite bearing metapelites. Lithos 334-335, 141–160.

Spear, F.S., Pyle, J.M., 2002. Apatite, monazite, and xenotime in metamorphic rocks. Phosphates 48, 293–335.
Stowell, H.H., Taylor, D.L., Tinkham, D.L., Goldberg, S.A., Ouderkirk, K.A., 2001. Contact metamorphic P–T–t paths from Sm–Nd garnet ages, phase equilibria modelling and thermobarometry: Garnet Ledge, south-eastern Alaska, USA. J. Metamorph. Geol. 19, 645–660.
Taghipour, S., Kananian, A., Harlov, D., Oberhansli, R., 2015. Kiruna-type iron oxide-apatite deposits, bafq district, central iran: fluid-aided genesis of fluorapatite-monazite-xenotime assemblages. Can. Mineral. 53 (3), 479–495.
Thomas, J.B., Watson, E.B., Spear, F.S., Shemella, P.T., Nayak, S.K., Lanzirotti, A., 2010. TitaniQ under pressure: the effect of pressure and temperature on the solubility of Ti in quartz. Contrib. Mineral. Petrol. 160, 743–759.
Tomkins, H.S., Pattison, D.R.M., 2007. Accessory phase petrogenesis in relation to major phase assemblages in pelites from the Nelson contact aureole, southern British Columbia. J. Metamorph. Geol. 25 (4), 401–421.
Trail, D., Savage, S.P., Moynier, F., 2019. Experimentally determined Si isotope fractionation between zircon and quartz. Geochim. et Cosmochim. Acta 260, 257–274.
Viskupic, K., Hodges, K.V., 2001. Monazite-xenotime thermochronometry: methodology and an example from the Nepalese Himalaya. Contrib. Mineral. Petrol. 141, 233–247.
Yardley, B.W.D., 2013. The chemical composition of metasomatic fluids in the crust. In: Metasomatism and the Chemical Transformation of Rock. Lecture Notes in Earth System Sciences. Springer, Berlin, Heidelberg.